Lehigh University
Lehigh Preserve

Theses and Dissertations

2017

An Integrated Method for Airfoil Optimization

Joshua Okrent
Lehigh University

Follow this and additional works at: http://preserve.lehigh.edu/etd

Part of the Mechanical Engineering Commons

Recommended Citation
Okrent, Joshua, "An Integrated Method for Airfoil Optimization" (2017). *Theses and Dissertations*. 2749.
http://preserve.lehigh.edu/etd/2749

This Thesis is brought to you for free and open access by Lehigh Preserve. It has been accepted for inclusion in Theses and Dissertations by an authorized administrator of Lehigh Preserve. For more information, please contact preserve@lehigh.edu.

An Integrated Method for Airfoil Optimization

Joshua Okrent

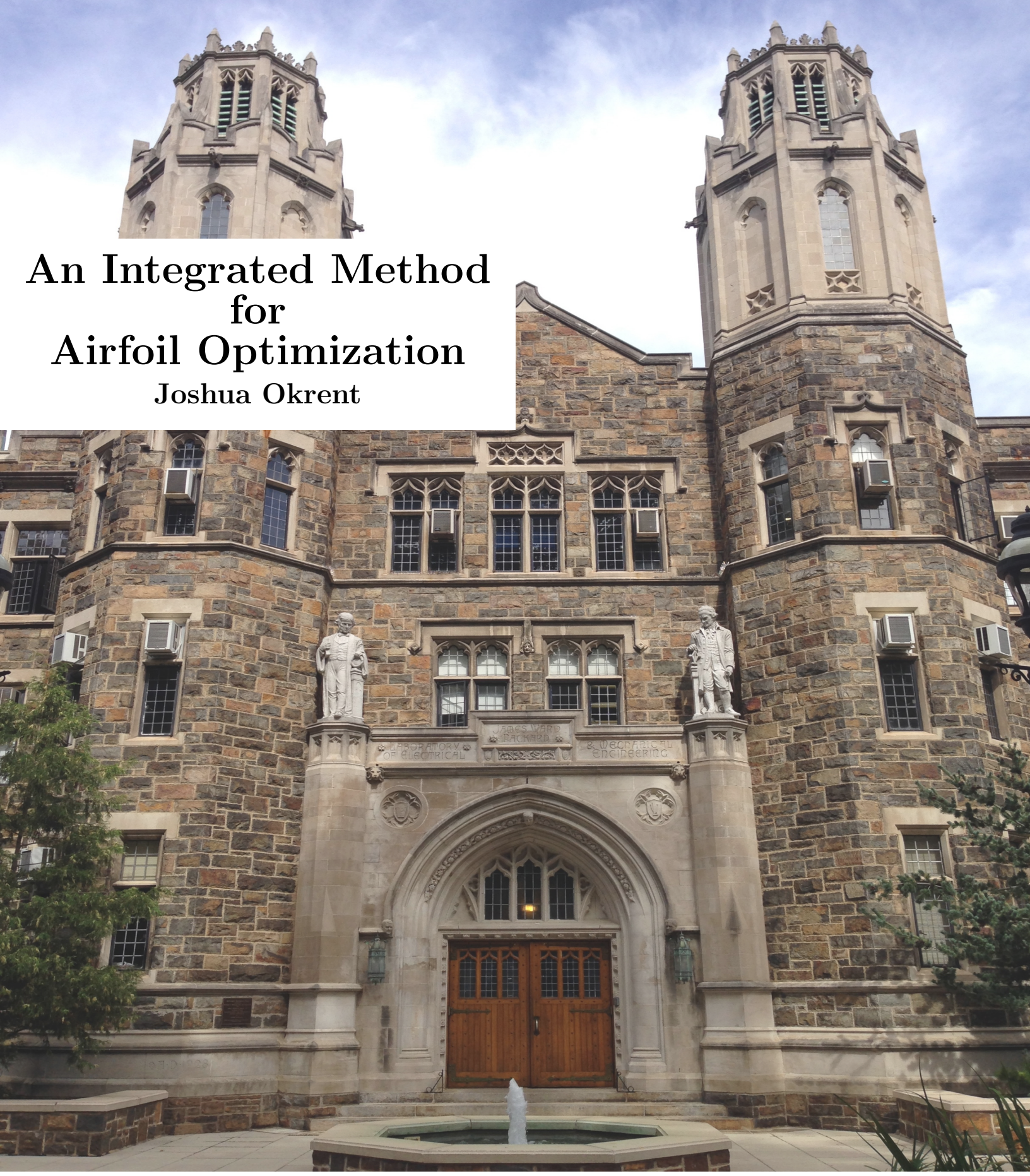

LEHIGH UNIVERSITY

An Integrated Method

for

Airfoil Optimization

by

Joshua B. Okrent

A Thesis

Presented to the Graduate and Research Committee

of

Lehigh University

In partial fulfillment of the

requirements for the degree of

Master of Science

in

Mechanical Engineering

May 2017

Copyright

©Copyright Joshua B. Okrent 2017

All Rights Reserved

Certificate of Approval

This thesis has been accepted and approved in partial fulfillment of the requirements of the degree of Master of Science in Mechanical Engineering.

Dr. Alparslan Oztekin Adviser	Date
Dr. Gary Harlow Department Chair	Date

Acknowledgements

There are many people who have helped me reach this goal and I am forever grateful for their help and support. First, I would like to thank Dr. Oztekin for acting as my adviser and his guidance and wisdom during my research. Second, I would like to thank my parents Aaron and Aileen Okrent for their continued support and love throughout my entire academic career. Last, I would like to thank my girlfriend Amalia Williams for her undying love and support. Without her help I would have been unable to finish this thesis.

Nomenclature

Dimensionless Numbers

Symbol	Description	Definition
η_p	Propeller Efficiency	
AR	Aspect Ratio	$\frac{b^2}{S}$
C_D	Coefficient of Drag	$\frac{F_D}{qS}$
c_d	2D Section Coefficient of Drag	$\frac{F_D}{qc}$
C_L	Coefficient of Lift	$\frac{F_L}{qS}$
c_l	2D Section Coefficient of Lift	$\frac{F_L}{qc}$
e	Oswald Efficiency Factor	
L/D	Lift-to-Drag Ratio	$\frac{C_L}{C_D}$
Re	Reynolds Number	$\frac{\rho V c}{\mu}$

Greek Symbols

Symbol	Description	Dimensions	Units

α	Angle of Attack		DEG
δ	Boundary Layer Height	L	m
μ	Viscosity	$ML^{-1}t^{-1}$	$Pa-s$
ϕ	Potential Function		
ρ	Density	ML^{-3}	kg/m^3

Roman Symbols

Symbol	**Description**	**Dimensions**	**Units**
b	Wing Span	L	m
c_p	Specific Fuel Consumption	$L^{-2}t^2$	$g/kW-h$
c	Chord Length	L	m
L	Drag Force	MLt^{-1}	N
E	Endurance	t	s
L	Lift Force	MLt^{-1}	N
R	Range	L	m
S	Wing Planform Area	L^2	m^2
$\vec{V}$	Velocity Vector	Lt^{-1}	m/s
V	Velocity Magnitude	Lt^{-1}	m/s
u	Velocity Component in the X Direction	Lt^{-1}	m/s
v	Velocity Component in the Y Direction	Lt^{-1}	m/s

w	Velocity Component in the Z Direction	Lt^{-1}	m/s

Abbreviations

CFD	Computational Fluid Dynamics
CIA	Centrial Intelligence Administration
GA	Genetic Algorithim
NACA	National Advisory Committee on Aeronautics
NASA	National Air and Space Administration
NOAA	National Oceanic and Atmospheric Administration
NS	Navier-Stokes
UAV	Unmanned Aerial Vehicle
UCAV	Unmanned Combat Aerial Vehicle
VI	Viscous Inviscid

Contents

Nomenclature **iv**

Abbreviations **vii**

List of Tables **xi**

List of Figures **xii**

Abstract **1**

1 Introduction **2**

1.1 Introduction 2

1.2 Objective 7

1.3 Structure 9

2 Problem Definition **10**

2.1 Optimization Problem 10

2.1.1 Airfoil Analysis 12

2.1.1.1 Performance Criteria 14

2.2 Planned Research 16

2.2.1 Analysis 16

2.2.2 Optimization 16

2.2.3 Candidate Airfoils 19
2.2.3.1 NACA 4 Digit 19
2.2.3.2 Class Shape Transformation 20
2.2.3.3 PARSEC 21

3 Description of Analysis 22

3.1 Introduction 22
3.2 Inviscid Flow 25
3.2.1 Panel Method Implementation 26
3.2.1.1 Panel Method Summary 30
3.3 Viscous Flow 31
3.3.1 The Incompressible Boundary Layer 32
3.3.2 The Compressible Boundary Layer 34
3.3.2.1 Closure 36
3.4 Coupled Viscous-Inviscid Solution 37
3.4.1 Direct Coupling 37
3.4.2 Quasi-Simultaneous 38
3.4.3 Simultaneous 38
3.5 XFOIL 39
3.6 Genetic Algorithm Settings 39

4 Results and Discussion 41

4.1 Introduction 41
4.1.1 NACA 4 Digit 42
4.1.2 CST 44
4.1.3 PARSEC 48

4.2 Comparison 50

5 Conclusion **52**

5.1 Further Work 54

References **55**

Curriculum Vitae **58**

List of Tables

2.1 Preliminary Aircraft Configuration 11

2.2 Endurance Mission Flight Profiles and Relative Weighting 11

2.3 Cruise Mission Flight Profiles and Relative Weighting 11

3.1 Genetic Algorithm Solver Input Parameters 40

4.1 Optimized NACA 4 Series Endurance Mission Performance 44

4.2 Optimized NACA 4 Series Range Mission Performance 44

4.3 Optimized CST Endurance Mission Performance 47

4.4 Optimized CST Range Mission Performance 47

4.5 Optimized PARSEC Endurance Mission Performance 50

4.6 Optimized PARSEC Range Mission Performance 50

4.7 Final Airfoil Scores 51

List of Figures

1.1 Francis G. Powers in Front of a U-2 Dragon Lady ([9]) 3

1.2 Infantryman launches a BirdEye 400 UAV 4

1.3 An MQ-9 Reaper Taxis on an Airstrip 5

1.4 Examples of Military Aircraft whose Missions are Increasingly Performed by UAV/UCAVs 6

2.1 Airfoil with Lift and Drag Vectors 12

2.2 Finite Wing with Wingtip Vortices and Elliptical Lift Distribution 13

2.3 Generation of Next Generation from Current Candidates ([12]) 18

2.4 NACA 2412 Airfoil in Normalized Coordinates 20

3.1 NACA 2412 Airfoil Discretized with 12 Panels 28

3.2 3D Paneling of Fighter Concept ([2]) 31

4.1 NACA 4 Series Fitness Function Score Convergence 42

4.2 Evolution of Optimal NACA 4 Series Airfoil 43

4.3 Final Optimized NACA 4 Series Airfoil 44

4.4 CST Fitness Function Score Convergence 45

4.5 Evolution of Optimal CST Airfoil 46

4.6 Final Optimized CST Airfoil 47

4.7 PARSEC Fitness Function Score Convergence 48

4.8 Evolution of Optimal PARSEC Airfoil 49

4.9 Final Optimized PARSEC Airfoil 50

4.10 Final Airfoil Shapes 51

Abstract

Design exploration and optimization is a large part of the initial engineering and design process. To evaluate the aerodynamic performance of a design, viscous Navier-Stokes solvers can be used. However this method can prove to be overwhelmingly time consuming when performing an initial design sweep. Therefore, another evaluation method is needed to provide accurate results at a faster pace. To accomplish this goal, a coupled viscous-inviscid method is used. This thesis proposes an integrated method for analyzing, evaluating, and optimizing an airfoil using a coupled viscous-inviscid solver along with a genetic algorithm to find the optimal candidate. The method proposed is different from prior optimization efforts in that it greatly broadens the design space, while allowing the optimization to search for the best candidate that will meet multiple objectives over a characteristic mission profile rather than over a single condition and single optimization parameter. The increased design space is due to the use of multiple parametric airfoil families, namely the NACA 4 series, CST family, and the PARSEC family. Almost all possible airfoil shapes can be created with these three families allowing for all possible configurations to be included. This inclusion of multiple airfoil families addresses a possible criticism of prior optimization attempts since by only focusing on one airfoil family, they were inherently limiting the number of possible airfoil configurations. By using multiple parametric airfoils, it can be assumed that all reasonable airfoil configurations are included in the analysis and optimization and that a global and not local maximum is found. Additionally, the method used is amenable to customization to suit any specific needs as well as including the effects of other physical phenomena or design criteria and/or constraints.

This thesis found that an airfoil configuration that met multiple objectives could be found for a given set of nominal operational conditions from a broad design space with the use of minimal computational resources on both an absolute and relative scale to traditional analysis techniques. Aerodynamicists, program managers, aircraft configuration specialist, and anyone else in charge of aircraft configuration, design studies, and program level decisions might find the evaluation and optimization method proposed of interest.

Chapter 1

Introduction

1.1 Introduction

Unmanned aerial vehicles (UAV) have been developed and used for reconnaissance and combat missions since the first World War. However, UAVs did not see any appreciable use until the avionics (portmanteau of aviation and electronics) matured enough to meet the requirements of such a demanding environment. Use of UAVs as combat reconnaissance platforms began to steadily increase during the Vietnam War as the capabilities of the avionics increased. This increase in use was also spurred in part, by the downing of the previously thought untouchable U-2 Dragon Lady manned reconnaissance platform piloted by Francis Gary Powers (Fig 1.1) on a CIA surveillance flight of the USSR.

Figure 1.1: Francis G. Powers in Front of a U-2 Dragon Lady ([9])

In the modern era, UAVs are used widely among all branches of the armed forces, intelligence agencies, federal, and local law enforcement agencies, as well as civilian agencies such as NASA and NOAA for gathering atmospheric and other flight data. They can vary in size and shape depending on the typical mission profile. Small UAVs such as Israel Aerospace Industries (IAI) Bird Eye (shown in Fig. 1.2) product line are small enough to be carried by an infantryman and are used for short distance reconnaissance of the battlefield. Depending on the configuration IAI's Bird Eye can weigh between 1.3 to 8.5 kg and stay aloft for 1-2 hours at a range of up to 10 kilometers. Such small man-portable UAVs provide real time information to the war fighter about the changing landscape of the battlefield that traditional information sources cannot. It also gives the individual war fighter unit the ability to gather information without needing the assistance of higher level units to give permission and coordinate the use of larger UAV resources.

Figure 1.2: Infantryman launches a BirdEye 400 UAV

On the other end of the scale are the larger and more well known UAVs colloquially referred to as drones since most possess capabilities to operate autonomously (or semi-autonomously) in addition to being operated by remotely located human pilots. One of the most well known large scale UAVs is the General Atomics MQ-9 Reaper (shown in Fig 1.3, is the successor to the smaller General Atomics MQ-1 Predator, and is occasionally termed Predator B).

Figure 1.3: An MQ-9 Reaper Taxis on an Airstrip

The MQ-9 is capable of high altitude, long endurance missions (HALE) and can carry 15 times the amount of ordnance, and cruise at three times the speed of the MQ-1 Predator. With its increased range, operational ceiling, endurance, speed, and munitions payload capability is the first large scale, true hunter-killer UAV, and is more aptly termed an unmanned aerial combat vehicle (UCAV) given its increased war fighting capabilities. UCAVs are increasingly being used in missions against soft targets (targets without the ability to contest air superiority as they do not have any combat aircraft or any anti-aircraft weapons capable of reaching the UCAV) such as ISIS, Al Qaeda, or other strategic targets since they have a significantly lower operating cost than other aerial combat vehicles such as the F-16 Fighting Falcon, F-18 Hornet (or Super Hornet variant), B-52, or A-10 Warthog (shown in Fig. 1.4) [11].

(a) F-16

(b) F-18

(c) B-52

(d) A-10

Figure 1.4: Examples of Military Aircraft whose Missions are Increasingly Performed by UAV/UCAVs

Without a doubt, use of UAVs and UCAVs will increase as they replace their manned counterparts for missions with soft targets. As their role (and number of units built and deployed) grows, so does the importance of optimizing the design of the UAV. What performance parameter that is desired to be optimized is dependent on the mission that the aircraft will be used for. Transport aircraft such as the C-5 or C-17 are designed to be able to move a large payload a long distance at a fuel efficient pace, whereas air superiority fighters like the F-15 Eagle or F-22 are optimized for speed and maneuverability among other things. This research project will focus on selecting the optimum airfoil for use on a UAV that is

nominally designed to be characteristic of the large scale HALE type UAV/UCAVs.

1.2 Objective

The objective of this study is to optimize an airfoil that is to be used for a long range, long endurance unmanned aerial vehicle UAV application. Since a VI coupled solver allows for an expedient and accurate solution, it is an excellent choice for an optimization problem where the number of design cases analyzed can range from 1,500-5,000+. To achieve the goal of being able to specify the best airfoil shape for a given aircraft design and set of flight conditions, the following steps will be taken:

- Select a characteristic UAV design.
- Create a characteristic mission condition matrix.
- Weight each mission condition by its relative importance.
- Select performance parameter(s) to optimize.
- Select a VII coupling method.
- Select a parametric airfoil family (ex. NACA 4 Digit Series).
- Couple the genetic algorithm solver (MATLAB) with the VI solver.
- Perform optimization.
- Repeat optimization with different parametric airfoil family (ex. NACA 5 digit series).
- Select the optimal airfoil.

This research differs from prior work for several reasons. First, most optimization work focuses on just one parametric airfoil family (ex. NACA 4 series) or even the more limited case of starting from a single airfoil (ex. NACA2412) and moving outward in the design space. Rather than be limited by a single parametric airfoil family, this work will use three different airfoil families that cover almost all (reasonable) design possibilities.

This change opens up a much larger design space allowing for the possibility of a better candidate to be found. Other approaches are limited since they start with a more limited pool of candidates. Another difference is the way the candidate airfoils are scored and evaluated. In prior work, most optimization methods searched for the candidate airfoil that provided the best lift-to-drag ratio for a given flight condition. For an airfoil that will be used on an aircraft with a very specific use where one flight condition overwhelmingly dominates all others, this single evaluation point approach works well. However, for any kind of aircraft with a varied mission flight profile, this approach finds an optimal candidate for just a small section of the expected flight conditions. This would be analogous to selecting a car based on its gas mileage performance on the highway when you mostly do city driving. The selection will still perform well, but it won't necessarily be the optimal choice to minimize total gas usage.

Additionally, the standard approach finds the optimal candidate based on one parameter only. When designing an airfoil or by extension an aircraft, there are many performance characteristics that are of importance. A better approach would be to evaluate each candidate airfoil with respect to several different performance characteristics that are relevant to the typical mission. For example, when designing a transport aircraft, both the fuel usage and maximum payload are of importance. Therefore, a more optimal design can be found when evaluating a design and finding the best option that both minimizes fuel usage and maximizes payload. For optimizations with multiple objectives, the optimization on any one performance characteristic can come at the expense of another performance characteristic.

It is up to the engineer to find the configuration that provides the best trade offs between performance characteristics. The optimization method used in this paper will be discussed in more detail in Chapter 2 and Chapter 3.

1.3 Structure

Chapter 2 will discuss the problem in more detail and will define the constraints and objectives. In addition, more information about UAVs will be provided.

Chapter 3 will discuss the method by which viscous and inviscid calculations are performed. It will also briefly discuss the coupling methods available.

Chapter 4 will present the results and discussion of the optimization solution.

Chapter 5 will provide concluding remarks as well as suggestions for further work.

Chapter 2

Problem Definition

2.1 Optimization Problem

For this design problem, it is assumed that the layout and configuration of a large scale high altitude, long endurance UAV has been determined from a list of mission requirements subject to structural and power plant constraints. Table 2.1 provides some nominal size and weight information for the UAV (characteristic of the HALE class of UAV). From this nominal aircraft configuration, it is up to the engineer to find the optimal airfoil that can maximize the UAV's performance. For this application, it is desired to optimize both the UAV's time on station (endurance), and it's range, or more simply how far the UAV can fly, and once it reaches its target, how long it can stay in the air.

Variable	**Unit**	**Value**
Empty Weight	kg	1247
Fuel Weight	kg	1769
Max. Payload	kg	1747
Max. Takeoff Weight	kg	4763
Wingspan	m	20
Chord	m	1.22
Aspect Ratio	N/A	12
Length	m	11

Table 2.1: Preliminary Aircraft Configuration

Additionally, since the UAV must operate at more than one flight condition, the optimal airfoil must be able to handle a variety of flight regimes and be able to perform. To evaluate the airfoil, a matrix of characteristic flight conditions was created. Each flight condition was weighted by the flight condition's relative importance. Any airfoil performance parameter is then defined as the weighted average of that parameter with respect to the weights in Tables 2.2 and 2.3. The weights for one flight regime each sum to one. For example, all of the condition weights in the cruise regime sum to one. In the next section, the endurance and range for a given airfoil is calculated as well as how a multi-objective optimization problem can be handled with a single objective function.

ID	Mission Description	Altitude. (km)	Velocity (m/s)	Mach No.	Re (10^6)	Weight
1	Low Alt. Loiter	5	35	0.109	1.93	0.20
2	Medium Alt. Loiter	10	40	0.134	1.38	0.50
3	High Alt. Loiter	15	45	0.153	0.75	0.30

Table 2.2: Endurance Mission Flight Profiles and Relative Weighting

ID	Mission Description	Altitude. (km)	Velocity (m/s)	Mach No.	Re (10^6)	Weight
1	Medium Alt. Cruise	10	110	0.367	3.81	0.60
2	High Alt. Cruise	15	110	0.373	1.84	0.40

Table 2.3: Cruise Mission Flight Profiles and Relative Weighting

2.1.1 Airfoil Analysis

In this section, airfoil and wing performance parameters will be briefly reviewed. It is assumed that the reader is already familiar with aerodynamics, thin airfoil theory, and performance analysis of an aircraft.

An airfoil (Fig. 2.1 is a 2D shape that when extruded or swept through space, forms a wing with finite span. A given airfoil has several performance properties associated with it.

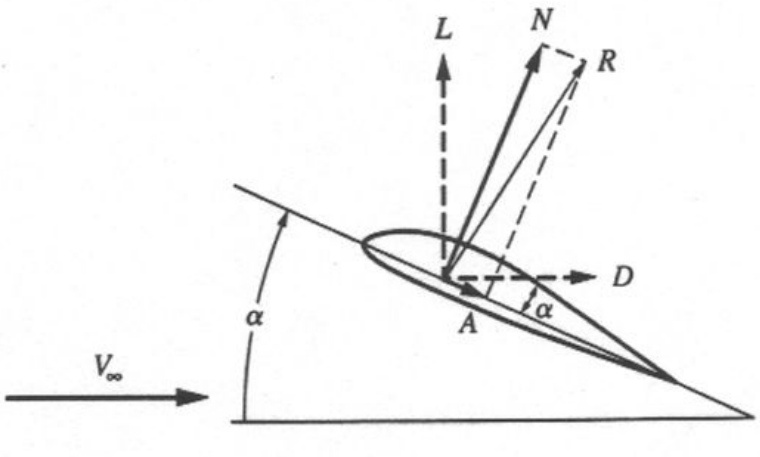

Figure 2.1: Airfoil with Lift and Drag Vectors

The two most important parameters are the non-dimensional lift and drag coefficients given in equations 2.1 and 2.2 respectively where l is the lifting force per unit span, d is the drag force per unit span, ρ is the density, and V_∞ is the free stream velocity. From thin airfoil theory, a given airfoil's c_l and c_d are a function of the angle of attack (α) of the airfoil relative to the free stream. The lift and drag coefficients provide quantitative metrics to measure an airfoil's performance and allow easy performance comparison across a wide swath of airfoil sizes and operating conditions.

$$c_l = \frac{l}{\frac{1}{2}\rho c V^2} \tag{2.1}$$

$$c_d = \frac{d}{\frac{1}{2}\rho c V^2} \tag{2.2}$$

While these two parameters provide good information to characterize an airfoil, they do not tell the whole picture when it comes to an actual wing of finite length. This is due in part to the additional induced drag, as well as the reduction in total lift from wingtip vortices (see Fig. 2.2).

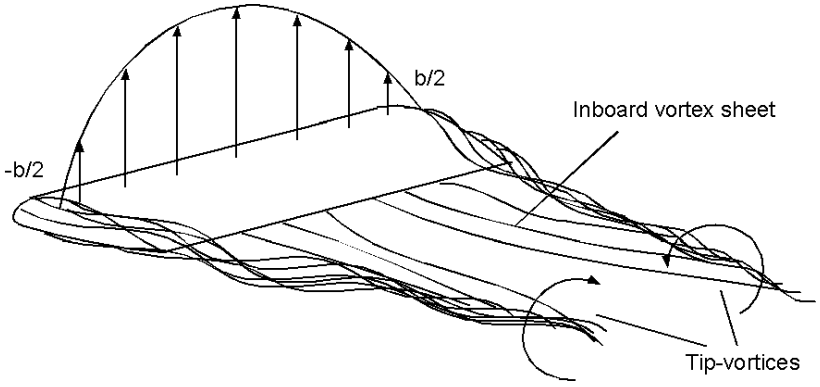

Figure 2.2: Finite Wing with Wingtip Vortices and Elliptical Lift Distribution

Working under the assumption of an elliptical lift distribution, it is possible to find the corrected lift and drag coefficients for a finite wing as shown in Equations 2.3 and 2.4.

$$C_L = \frac{L}{\frac{1}{2}\rho S V^2} = \frac{c_l}{1 + \frac{c_l}{1+\pi e AR}} \tag{2.3}$$

$$C_D = \frac{D}{\frac{1}{2}\rho S V^2} = c_d + \frac{C_L^2}{\pi e AR} \tag{2.4}$$

where S is the wing planform area, e is the non-dimensional Oswald efficiency

number (usually 0.80-0.95) and AR is the wing aspect ratio defined as the ratio of the square of the wingspan divided by the planform area. For a rectangular wing, the aspect ratio is simply the wingspan divided by the chord length.

2.1.1.1 Performance Criteria

It is possible to achieve a good engineering approximation (usually within 10-20%) of an aircraft's endurance (E) and range (R) using the Breguet formula (equation 2.5 and 2.6 where c_p is the specific fuel consumption, η_p is the propeller efficiency, ρ_∞ is the free stream density, S is the wing planform area, W_i is the initial weight of the aircraft, W_f is the final weight of the aircraft, and C_L and C_D are the lift and drag coefficients respectively)[1].

$$E = \frac{\eta_p}{c_p}\frac{C_L^{\frac{3}{2}}}{C_D}\sqrt{2\rho S}\left(\frac{1}{\sqrt{W_f}} - \frac{1}{\sqrt{W_i}}\right) \tag{2.5}$$

$$R = \frac{\eta_p}{c_p}\frac{C_L}{C_D}\ln\frac{W_i}{W_f} \tag{2.6}$$

$$\tag{2.7}$$

Since the design of the airfoil can only affect C_L or C_D,if an airfoil maximizes the value of

$$\frac{C_L^{\frac{3}{2}}}{C_D}$$

or

$$\frac{C_L}{C_D}$$

then for a given weight and power plant configuration, the endurance or range

has been maximized. Since there are two competing objectives (maximize endurance and maximize range) , a method to accommodate both goals must be used. One could perform a multi-objective genetic algorithm based optimization, from which a candidate could be selected from the set of generated airfoils on the Pareto front. A simpler method is to weight each objective and then minimize the sum of the weighted objectives, which is the method used in this research [3]. In more explicit mathematical terms:

$$\text{minimize } \mathbf{f} = \sum_{i=1}^{N} w_i f_i(\mathbf{x}) \tag{2.8}$$

$$\text{subject to } \mathbf{x} \in \Omega \tag{2.9}$$

This approach requires some knowledge or assumptions about what the respective weights should be [3] and the solution may or may not be strongly dependent on the weights chosen. For this research, it will be assumed that 80% of the UAV's flight time will be spent in endurance mode, and 20% of the UAV's flight time will be spent in cruise mode and the objectives should be weighted accordingly, which gives the following objective function $\mathbf{f}$ which is to be minimized.

$$\text{minimize } \mathbf{f} = \frac{4}{5}\left(\sum_{i=1}^{N_E} w_{E,i}\frac{C_L^{\frac{3}{2}}}{C_D}\right)^{-1} + \frac{1}{5}\left(\sum_{i=1}^{N_R} w_{R,i}\frac{C_L}{C_D}\right)^{-1} \tag{2.10}$$

$$\text{subject to } \mathbf{x} \in \Omega \tag{2.11}$$

where N_E and N_R are the number of endurance and range conditions to be evaluated and $w_{E,i}$ and $w_{R,i}$ are their associated condition weights from Table 2.2-2.3. In this application, $\mathbf{x}$ is the vector of parameters that is used to define a given parametric airfoil

family (ex. camber, location of camber maximum, and thickness for a NACA 4 series airfoil) and Ω is the bounds on that set of parameters than give a valid airfoil.

2.2 Planned Research

2.2.1 Analysis

The airfoil shape in question will be analyzed using the coupled viscous-inviscid code XFOIL. XFOIL will be treated like a black box function to which the airfoil shape and flight conditions are passed to, and from which the sectional lift and drag coefficients will be returned. Using equations 2.3, 2.4, and the values given in Table 2.1, the finite wing lift and drag coefficients will be determined. Once the values of C_L and C_D are known, $\frac{C_L^{\frac{3}{2}}}{C_D}$ and $\frac{C_L}{C_D}$ can be found, and the airfoil can be scored using the objective function listed in Equations 2.10-2.11. Chapter 3 will briefly cover the basics of the viscous-inviscid calculations and coupling method used by XFOIL in it's calculation of c_l and c_d for an arbitrary airfoil shape.

2.2.2 Optimization

There are many ways to optimize a given problem. For example, a simple problem that can be modeled using a parabolic equation can be minimized by simply finding the roots of the function's derivative. More complex problems, but ones that are still governed by clear equations might be amenable to optimization through the use of Lagrange multipliers. Such approaches do not work as well when applied to the design problem at hand, namely since the equations that determine the airfoil's performance as a function of airfoil geometry are not that simple to solve. Additionally, since the method of solving those equations (XFOIL) is treated as a black box function so any methods that involve determining gradients is not

viable. For this reason, genetic algorithm optimization method was chosen.

A genetic algorithm is an optimization method that is appropriate for finding global minima for constrained and unconstrained problems using a scoring and sorting method that attempts to replicate an evolutionary process. A genetic algorithm is a good method for problems that are not appropriate for traditional optimization methods, including problems that have objective functions that are non-linear, stochastic, non-differentiable, or discontinuous. A general implementation of a genetic algorithm follows these steps [12]:

1. Generate (random) initial population based on vector of design parameters.
2. Compute the fitness score of each member of the population.
3. Select a certain subgroup of the population to become parents for the next generation based on their fitness score.
4. Select a certain subgroup of the population (termed elites) to be passed directly to the next generation based on their fitness score.
5. Produce children candidates from the parent candidates by:
   (a) Mutating the design parameters of a single parent candidate using a random number generator.

   or

   (b) Creating a linear combination of the design parameters of two parent candidates.
6. Combine the children candidates with the elite candidates to form the next generation.
7. Repeat the process until a convergence parameter is reach.

Individual implementations of a genetic algorithm can vary and the number of parameters used, the size of each population as well as number of elite, mutated, and crossover children candidates can either hasten or slow convergence. For a graphical explanation of how the next generation of candidates are created from the current one, see Figure 2.3. The details and the exact implementation of a genetic algorithm implementation are outside the scope of this research and will not be discussed.

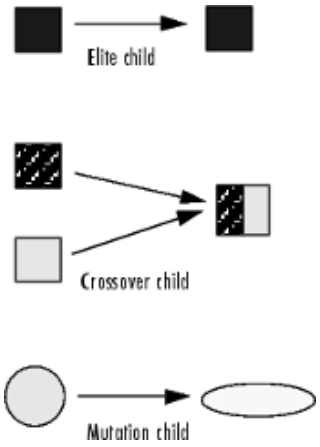

Figure 2.3: Generation of Next Generation from Current Candidates ([12])

The implementation of a genetic algorithm optimization method that was used for this research was provided by Matlab via their optimization toolbox. Below is the general work flow inside the objective function once a candidate airfoil has been passed to it for scoring and evaluation:

1. Receive candidate airfoil information from genetic algorithm solver.
2. Compute the fitness score for the candidate (Equation 2.10).
   (a) Pass the airfoil coordinates and flight conditions to XFOIL.
   (b) Return c_l and c_d from XFOIL.
   (c) Compute C_L and C_D from c_l and c_d.
   (d) Repeat the process for each unique flight condition.
3. Return the inverse of the candidate's fitness score.

Matlab's genetic algorithm can only minimize a quantity, so to find the design candidate that has the best (maximum) objective function score, the inverse of a candidate airfoil's score is returned to the GA solver. The solver then finds the set of airfoil parameters that minimizes this quantity, which then maximizes the weighted objective function. .

2.2.3 Candidate Airfoils

To use the genetic algorithm solver, an airfoil must be parametrized such that a vector of parameters is enough to fully define it's shape. To accomplish this goal, one must need use a parametric airfoil. There are several different commonly used parametric airfoil families that vary in their level of geometry control and complexity of implementation. Three of these airfoil families were selected to provide a large possibility of options when searching for the optimal configuration. The following sections will briefly discuss the three families of parametric airfoils that were used for this research.

2.2.3.1 NACA 4 Digit

One of the most basic methods of airfoil parametrization is the NACA 4 digit series of airfoils. Created by the National Advisory Committee for Aeronautics (NACA), this family of airfoils requires only three parameters (maximum camber, maximum camber location, and maximum thickness) to fully define the geometry. Traditionally these values are provided as percentages that have been normalized to the chord length of the airfoil. Additionally the values of the parameters drive the naming scheme of that airfoil itself. For example, a NACA 2412 airfoil (shown in Fig. 2.4 has a maximum camber of 2% chord located at 40% of the chord length and maximum airfoil thickness of 12% thickness. Usually, the airfoil shapes were defined only for certain integer values (ex. increments of 10% for maximum camber) but the equations that define the shape of the airfoil can accept any real valued positive chord normalized value. For example, the governing equation can generate an airfoil with a maximum camber of 23.67% located at 42.31% of the chord and normalized thickness of 12.23%. This flexibility allows for a much larger design space than is normally specified.

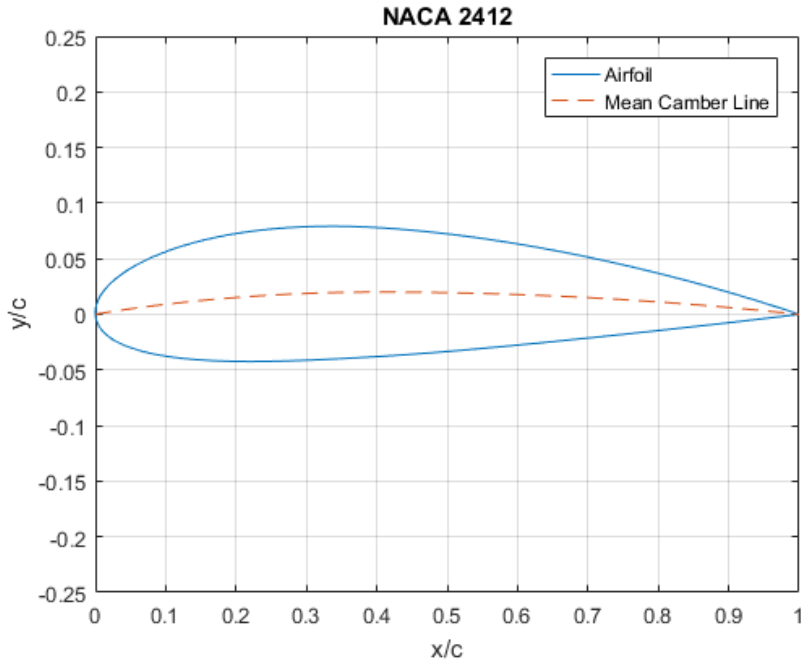

Figure 2.4: NACA 2412 Airfoil in Normalized Coordinates

2.2.3.2 Class Shape Transformation

The class shape transformation (CST) method is a parametric method for generation airfoil geometry with a limited number of parameters. It utilizes a series of class functions that are defined for certain geometries (round nose airfoils, low drag projectiles, cone etc) as well as shape functions for each geometry type to generate airfoil coordinates. The CST method was first presented by Brenda M. Kulfan while working for The Boeing Company. It can be used to parametrically describe airfoils, nacelles, lifting bodies, channels, ducts, nozzles and more in both two and three dimensions [4]. This flexibility makes it attractive for a large scale design optimization since a minimal number of parameters are needed to fully define a large system.

2.2.3.3 PARSEC

The third and final parametric geometry creation method used in this research is the PARSEC method as defined by Sobieczky [21]. The PARSEC method uses 11 airfoil parameters to fully define the airfoil geometry. These parameters are:

1. Leading edge radius.
2. Maximum height of the upper surface from the chord line.
3. X location of the maximum upper surface height.
4. Curvature at that location.
5. Maximum height of the lower surface from the chord line.
6. X location of the maximum lower surface height.
7. Curvature at that location.
8. Upper surface trailing edge angle.
9. Lower surface trailing edge angle.
10. Trailing edge thickness.
11. Trailing edge elevation.

The height of the airfoil surface is then given by equation 2.12.

$$\frac{y}{c} = \sum_{n=1}^{6} a_n(\vec{p}) x^{n-0.5} \tag{2.12}$$

where $\vec{p}$ is the vector containing the 11 governing parameters, a_n is the coefficients determined for $\vec{p}$. The value of a_n is determined by solving a set of linear equations. For more information on how to find the values of the coefficients see Jung et al. [14].

Chapter 3

Description of Analysis

3.1 Introduction

An engineer tasked with analyzing the flow of a fluid around a structure has a number of tools at their disposable. The tool they choose can greatly influence both the computational cost (man hours required to use the tool and/or monetary cost needed to acquire the tool itself) and the accuracy of the result itself. The intelligent engineer should choose the tool that meets the minimum solution accuracy requirement at the lowest computational cost. For example, a complex flow such as that of an unsteady, turbulent thermal fluid with volumetric heating through a nuclear reactor core might require a costly, but more accurate and capable computational fluid dynamics (CFD) Navier-Stokes (NS) equations solver such as ANSYS FLUENT to provide accurate information. Acquisition costs of the software alone are on the magnitude of $30,000. When one takes into account the cost of training an engineer to use the tool as well as the time it takes to perform an analysis, one would attempt to find another tool that can provide accurate engineering information at a lower cost. For flows with simple geometry such as a flat plate or sphere, an engineer

might defer to empirical correlations which can provide accurate information at cost that is several orders of magnitude less.

For engineering flows where the wall geometry cannot be fully defined in terms of a few characteristic dimensions (ex. a right cylinder needs only a diameter and length), empirical correlations become less useful. For this case, a fully viscous flow solver can be used, but the wall geometry and/or flow physics might be simple enough that a solution may be found with a simplified method at a lower computational cost. For this kind of flow regime, potential flow theory can provide good enough information to be able to characterize the flow.

Since potential flow assumes the fluid is inviscid, solution information will not be as accurate as information provided by a viscous NS solver especially in the vicinity of the wall. This decrease in accuracy is due to the fact that when a fluid flow impinges on or contacts a solid (or porous) surface, the component of the fluid velocity that is tangential to the surface normal vector is reduced to the velocity of that surface. For stationary walls, this means the tangential component of the velocity is reduced to zero. This phenomena is termed the no slip condition and is a valid assumption in the majority of flows. The no-slip condition causes a velocity gradient proportional to $\sqrt{Re}$ in the direction normal to the wall surface, where Re is the non-dimensional Reynolds number. Potential flow solvers do not account for any disturbances caused by the boundary layer since they do not include viscosity. For external aerodynamic flows, the Reynolds number is on the order of $10^5 - 10^7$ making it large enough to noticeably affect the difference between calculated and actual flow information. For aerodynamic flows, this is especially important since the calculated drag on an airfoil from potential flow is much lower than the actual drag found from experiments.

Using a viscous NS solver to resolve the boundary layer can be computationally prohibitive especially if turbulence is present for large models. To properly resolve the boundary layer in viscous NS solvers, the mesh near the wall needs to be discretized such

that the element height measured normal to the wall surface must be quite small. This mesh sizing requirement not only adds significant computational cost, it adds significant time to the pre-processing step since special care must be taken to discretize the domain near the wall. This step increases in complexity again when turbulence is discretized to be modeled since the non-dimensional cell height $y+$ must be matched to the required $y+$ of the turbulence model used. This matching process can take a few solution iterations before inflation parameters that yield the desired $y+$ are found. Although a solution found with a viscous NS solver (when setup correctly) will yield more accurate results, the added cost again warrants caution, especially when a variety of geometries and design cases need to be evaluated.

Thankfully, a method to include boundary layer effects in the computationally inexpensive inviscid panel method exists. This method is termed the viscous-inviscid (VI) coupling and relies on the integral boundary layer formulation pioneered by Prandtl and von Karman.

This VI coupling provides a powerful tool that can accurately predict the aerodynamic flows when compared to fully gridded viscous NS solver or laboratory experiments. Implementations of a VI coupling code run in milliseconds on a modern computer which is orders of magnitude faster than the run time of even a simple 2D airfoil in a viscous NS solver. This speed and ease of use makes it ideal for preliminary design analysis and optimization, especially once turbulence and compressibility effects are included.

This chapter will briefly discuss some of the common ways to solve the inviscid, viscous, and coupled problem as well as provide some overview into the details of the solver that was used (XFOIL).

3.2 Inviscid Flow

For external flows that have a sufficiently large Reynolds number ($Re > 100,000$), it is a valid engineering approximation to assume that the flow outside of a small region near the wall surface is inviscid. We then define a potential function $\phi(x, y, z)$ and stipulate that it satisfies the requirements of conservation of mass and momentum. It is also assumed that the flow is steady, inviscid, irrotational, and incompressible. We also define the velocity components of $\vec{V}$ to be:

$$u = \frac{\partial \phi}{\partial x} \tag{3.1}$$

$$v = \frac{\partial \phi}{\partial y} \tag{3.2}$$

$$v = \frac{\partial \phi}{\partial z} \tag{3.3}$$

Since we have assumed that the flow is incompressible, the continuity equation is reduced to:

$$\nabla \cdot \vec{V} = \frac{\partial u}{\partial x} + \frac{\partial v}{\partial y} + \frac{\partial w}{\partial z} = 0 \tag{3.4}$$

We then substitute our equations for the velocity components as functions of the potential function into the continuity equation which yields the familiar Laplace equation.

$$\frac{\partial^2 \phi}{\partial x^2} + \frac{\partial^2 \phi}{\partial y^2} + \frac{\partial^2 \phi}{\partial z^2} = \nabla^2 \phi = 0 \tag{3.5}$$

It is more convenient to represent the flow with the potential function since ϕ

contains all of the information necessary to specify u, v, or w. Additionally, we can represent a variety of elementary flows with simple potential functions. Since the Laplace equation is linear, any number of solutions can be superimposed to form a valid, but more complex flow field.

Airfoils can be modeled and analyzed using just a few of the elementary potential flows. In thin airfoil theory, an airfoil is modeled by placing a bound vortex sheet along the mean camber line [15]. The vortex strength is then adjusted until the mean camber line becomes a streamline of the flow. Applying the Kutta condition which stipulates that the flow leaving the trailing edge must do so smoothly ($\gamma(TE) = 0$) which yields a unique solution. The main focus of thin airfoil theory is to find a γ distribution that satisfies the Kutta condition as well as the requirement the normal components of the uniform stream velocity and induced velocity must sum to zero[15]. Analytical solutions for both symmetric and cambered airfoils can be found once several geometric simplifications are made. For more information on the mathematical steps see Kuethe and Chow.

3.2.1 Panel Method Implementation

Thin airfoil theory does not work well for thick, highly cambered, multi-part, or arbitrary airfoil sections. To get around this issue, a source-panel method for solving the potential flow is used. This method is similar to the bound vortex sheet method of thin airfoil theory, however it also adds a source component to the airfoil. To begin with, the airfoil geometry is approximated by N line segments called panels. Each panel is assigned a fictitious source (q) and vortex (γ). The velocity potential function is created by superimposing the contributions from the free stream, source distribution, vortex distribution, which gives Equation 3.6 as viewed by an observer located in the fluid [18]. By solving for each panel's source and vortex strength, the velocity potential function can be solved to provide

the pressure distribution and section lift coefficients.

$$\phi = V_\infty(x\cos\alpha + y\sin\alpha) + \sum_{j=1}^{N}\int_j \Big(\frac{q_j}{2\pi} lnr - \frac{\gamma}{2\pi}\theta\Big)ds \tag{3.6}$$

The velocity potential due to the source and vortex distribution is integrated over the j-th panel element with length ds, where r is the distance between the element and the observer, and θ is the angle r makes with the x axis. This value is then summed over all of N panel elements. The following assumptions are made about the vortex and source distributions.

1. Source strength is constant over each panel.
2. Each panel has a different source strength.
3. Vortex strength is constant and equal across all panels.

The j-th panel has its start point denoted by (x_i, y_i) and its endpoint denoted by (x_{i+1}, y_{i+1}).Each panel has several important parameters used in calculating the strength of the distributed sources and vortex. These parameters are the location of the panel midpoint (Equation 3.7), it's length (Equation 3.8), and angle of orientation (Equation 3.9 and 3.10).

$$(\bar{x}_j, \bar{y}_j) = \Big(\frac{x_i + x_{i+1}}{2}, \frac{y_i + y_{i+1}}{2}\Big) \tag{3.7}$$

$$\ell_j = \sqrt{(x_{i+1} - x_i)^2 + (y_{i+1} - y_i)^2} \tag{3.8}$$

$$\sin\theta_j = \frac{y_{i+1} - y_i}{\ell_j} \tag{3.9}$$

$$\cos\theta_j = \frac{x_{i+1} - x_i}{\ell_j} \tag{3.10}$$

The midpoint of the panel is termed the collocation or control node. This is where

all of the sources and vortices are assumed to be acting on. Fig. 3.1 shows an example of how an airfoil might be paneled as well as the location of its collocation nodes.

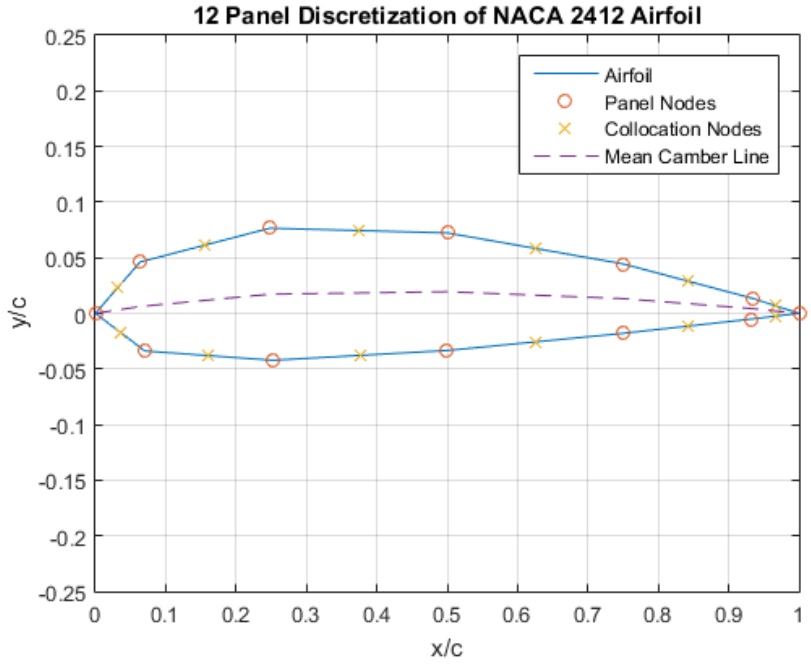

Figure 3.1: NACA 2412 Airfoil Discretized with 12 Panels

The no penetration condition enforced at the collocation point of each panel yields the following set of equations:

$$\sum_{j=1}^{N} q_j A_{ij} + \gamma A_{i,N+1} = b_i \text{ for } i = 1, ..., N \tag{3.11}$$

where

$$A_{ij} = \frac{1}{2\pi}\sin(\theta_i - \theta_j)\ln\left(\frac{r_{i,j+1}}{r_{ij}}\right) + \frac{1}{2\pi}\beta_{ij}cos(\theta_i - \theta_j) \tag{3.12}$$

$$A_{i,N+1} = \sum_{j=1}^{N}\left[\frac{1}{2\pi}\cos(\theta_i - \theta_j)\ln\left(\frac{r_{i,j+1}}{r_{ij}}\right) - \frac{1}{2\pi}\beta_{ij}\sin(\theta_i - \theta_j)\right] \tag{3.13}$$

$$b_i = V_\infty \sin(\theta_i - \alpha) \tag{3.14}$$

Finally, the Kutta condition is enforced which allows for closure of the system of equations.

$$\sum_{j=1}^{N} q_j A_{N+1,j} + \gamma A_{N+1,N+1} = b_{N+1} \tag{3.15}$$

where

$$A_{N+1,j} = \sum_{k=1,N} \left[\frac{1}{2\pi} \beta_{kj} \sin(\theta_k - \theta_j) - \frac{1}{2\pi} \cos(\theta_k - \theta_j) \ln\left(\frac{r_{i,j+1}}{r_{ij}}\right) \right] \tag{3.16}$$

$$A_{N+1,N+1} = \sum_{k=1,N} \sum_{j=1}^{N} \left[\frac{1}{2\pi} \beta_{kj} \cos(\theta_k - \theta_j) - \frac{1}{2\pi} \sin(\theta_k - \theta_j) \ln\left(\frac{r_{i,j+1}}{r_{ij}}\right) \right] \tag{3.17}$$

$$b_{N+1} = -V_\infty \cos(\theta_1 - \alpha) - V_\infty \cos(\theta_N - \alpha) \tag{3.18}$$

The values of r_{ij} and β_{ij} can be found from Equations 3.19 and 3.20 respectively.

$$r_{ij} = \sqrt{(\bar{x}_i - x_j)^2 + (\bar{y}_i - y_j)^2} \tag{3.19}$$

$$\beta_{ij} = \begin{cases} \text{atan2}\left[\begin{array}{l} (\bar{y}_i - y_{j+1})(\bar{x}_i - x_j) - (\bar{x}_i - x_{j+1})(\bar{y}_i - y_j), \\ (\bar{y}_i - y_{j+1})(\bar{y}_i - y_j) - (\bar{x}_i - x_{j+1})(\bar{x}_i - x_j)) \end{array} \right] & i \neq j \\ \pi & i = j \end{cases} \tag{3.20}$$

The function $\text{atan2}(Y, X)$ is defined as the four quadrant inverse tangent that returns values in the closed interval $[-\pi, \pi]$ based on the values of Y and X. The four quadrant

inverse tangent is used over the regular inverse tangent function so that the correct angle is returned. Now that the full system of linear equations has been defined, the strength of the fictitious distributed sources and vortex can be found. Once those are found it is possible to find the value of the tangential velocities at each control point, and from there use the Bernoulli equation to find the pressure distribution [17].

$$\begin{aligned} V_{t,i} =& V_\infty \cos(\theta_i - \alpha) \\ &+ \sum_{j=1}^{N} \frac{q_j}{2\pi} \left[\beta_{ij} \sin(\theta_i - \theta_j) - \cos(\theta_i - \theta_j) \ln\left(\frac{r_{i,j+1}}{r_{ij}}\right) \right] \\ &+ \frac{\gamma}{2\pi} \sum_{j=1}^{N} \left[\sin(\theta_i - \theta_j) \ln\left(\frac{r_{i,j+1}}{r_{ij}}\right) + \beta_{ij} \cos(\theta_i - \theta_j) \right] \end{aligned} \tag{3.21}$$

$$p_\infty + \frac{1}{2}\rho V_\infty^2 = p_i + \frac{1}{2}\rho V_{t,i}^2 \tag{3.22}$$

$$C_{p,i} = 1 - (\frac{V_{t,i}}{V_\infty})^2 \tag{3.23}$$

3.2.1.1 Panel Method Summary

Once implemented with a computer routine, the panel method provides a quick and easy way to find the tangential velocity and pressure distributions over an airfoil of an arbitrary shape, and from there the lift coefficients. Results converge fairly rapidly exhibiting little change once the number of panels used exceeds approximately 60 [17]. Although the process demonstrated above was only for the two dimensional case, the panel method can be expanded to include three dimensions (example shown in Figure 3.2) and account for compressibility effects as well. Some proprietary panel method implementations such as Boeing's PANAIR and Douglas' HESS II code allow for curved panels, and non constant

source and vortex terms [17]. For a more in depth comparison of different available panel codes see Table 4-3 of [17].

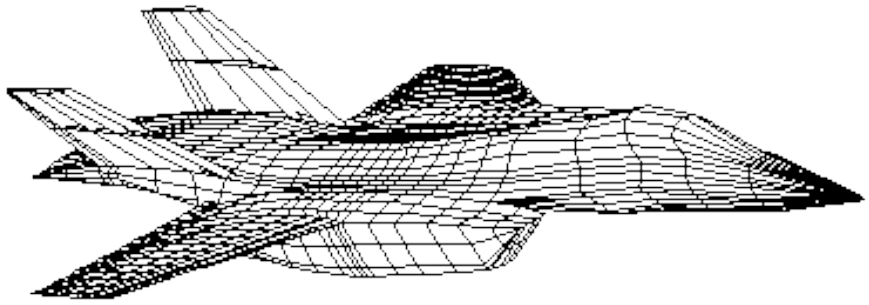

Figure 3.2: 3D Paneling of Fighter Concept ([2])

The panel method produces inviscid solutions that closely match experimental results. This agreement, however rapidly deteriorates as the angle of attack of the airfoil increases until the airfoil is fully stalled [17].The panel method cannot accurately predict results from this flow regime, rather it will continue to predict a linear increase in lift. Therefore, without any adulterations to the analysis process, one should take care to make sure the conditions they are analyzing are within the valid limits of the panel method.When one keeps the various restrictions of the panel method in mind, it still makes an attractive high level analysis tool due to it's ease of use, extreme speed, and relative accuracy.

3.3 Viscous Flow

For regions near the wall surface, the assumption of irrotational and inviscid flow are no longer valid. For this reason, the viscous boundary layer equations need to be solved. In this section, a method to solve for the flow in an incompressible laminar boundary layer is presented.

3.3.1 The Incompressible Boundary Layer

We start with the classical form of Prandtl's boundary layer equation and the reduced form of the continuity equation (equations 3.24 and 3.25). The subscripts 1 and 2 denote the coordinate parallel and normal to the wall surface respectively.

$$u_1\frac{\partial u_1}{\partial x_1} + u_2\frac{\partial u_1}{\partial x_2} = -\frac{1}{\rho}\frac{\partial p}{\partial x_1} + \nu\frac{\partial^2 u_1}{\partial x_2^2} \tag{3.24}$$

$$\frac{\partial u_1}{\partial x_1} + \frac{\partial u_2}{\partial x_2} = 0 \tag{3.25}$$

We make the assumption that the pressure gradient can be found from the Bernoulli equation and is given by:

$$\frac{\partial p}{\partial x_1} = -\rho U_\infty \frac{dU_\infty}{dx_1} \tag{3.26}$$

We transform Prandtl's boundary layer equation into an integral form by first manipulating the second term of equation 3.24 and then substituting the continuity equation to create the result shown in equation 3.27.

$$u_2\frac{\partial u_1}{\partial x_2} = \frac{\partial}{\partial x_2}(u_1u_2) - u_1\frac{\partial u_2}{\partial x_2} = \frac{\partial}{\partial x_2}(u_1u_2) + u_1\frac{\partial u_1}{\partial x_1} \tag{3.27}$$

Then equation 3.26 and 3.27 are substituted into equation 3.24 and by integrating from $x_2 = 0$ to $x_2 = \delta$ where δ is the total boundary layer thickness, subject to the boundary conditions $x_2 = 0, u_1, u_2 = 0$ and $u_2 = \delta, u_1 = U_\infty(u_1)$ [20]. This procedure yields an ordinary differential equation, known as the Von Karman integral momentum equation.

$$\int_0^\delta u_1 2\frac{\partial u_1}{\partial x_1}dx_2 + \int_0^\delta \frac{\partial}{\partial x_2}(u_1u_2)dx_2 = \int_0^\delta U_\infty \frac{dU_\infty}{dx_1}dx_2 + \nu\int_0^\delta \frac{\partial^2 u_1}{\partial x_2^2}dx_2 \tag{3.28}$$

To facilitate the evaluation of equation 3.28, we treat each term separately and simplify their form.

$$\int_0^\delta 2u_1\frac{\partial u_1}{\partial x_1}dx_2 = \int_0^\delta \frac{\partial(u_1^2)}{\partial x_1}dy \tag{3.29}$$

$$\int_0^\delta \frac{\partial}{\partial x_2}(u_1u_2)dx_2 = -U_\infty\int_0^\delta \frac{\partial u_1}{\partial x_1} \tag{3.30}$$

$$\int_0^\delta \frac{\partial^2 u_1}{\partial x_2^2}dx_2 = \frac{\partial u_1}{\partial x_2}\Big|_{x_2=0} = -\frac{\tau_w}{\rho} \tag{3.31}$$

Equations 3.29-3.31 are substituted back into equation 3.28 and then by making the assumption that U_∞ is not a function of x_2 and using some tricks from calculus (integration by parts and Leibniz's rule) it is possible to rearrange the result such that is now of the form:

$$\frac{\partial}{\partial x_1}\left[U_\infty^2\int_0^\delta \frac{u_1}{U_\infty}\Big(1-\frac{u_1}{U_\infty}\Big)dx_2\right] + U_\infty\frac{dU_\infty}{dx_1}\int_0^\delta \Big(1-\frac{u_1}{U_\infty}\Big)dx_2 = \frac{\tau_w}{\rho} \tag{3.32}$$

By noticing that the integrand of the first term is the definition of θ, the momentum thickness, and the integrand of the second term is equal to the definition of δ^*, the displacement thickness, and by introducing another dimensionless shape parameter $H = \frac{\delta^*}{\theta}$the integral momentum equation can be reduced again to:

$$\frac{d\theta}{dx_1} + \Big(H + 2\Big)\frac{\theta}{U_\infty}\frac{dU_\infty}{dx_1} = \frac{C_f}{2} \tag{3.33}$$

Equation 3.33 represents the Von Karman momentum integral equation in differential form for incompressible flow and is an exact equation [20]. Solutions may be found by assuming a similarity function for the velocity profile, or by using a velocity profile from an inviscid panel method solution.

3.3.2 The Compressible Boundary Layer

The compressible boundary layer formulation in this section follows that of presented by Drela and Giles [8]. A similar approach that was used in the prior section was used to derive the standard integral momentum and kinetic energy shape parameter equations that are shown below:

$$\frac{d\theta}{dx_1} + \Big(2 + H - M_e^2\Big)\frac{\theta}{U_\infty}\frac{dU_\infty}{dx_1} = \frac{C_f}{2} \tag{3.34}$$

$$\theta\frac{dH^*}{dx_1} + \Big(2H^{**} + H^*(1 - H)\Big)\frac{\theta}{U_\infty}\frac{dU_\infty}{dx_1} = 2C_{Di} - H^*\frac{C_f}{2} \tag{3.35}$$

where M_e is the Mach number at the edge of the boundary layer, and C_{Di} is the dissipation coefficient. The definitions of the dissipation coefficient, kinetic energy, and density thickness for compressible flow are defined in a similar manner to their incompressible counterparts [19].

$$\theta^* = \int_0^\infty \left(1 - \left(\frac{u_1}{U_\infty}\right)^2\right) \frac{\rho u_1}{\rho U_\infty} dx_2 \tag{3.36}$$

$$\delta^{**} = \int_0^\infty \left(1 - \left(\frac{\rho}{\rho_\infty}\right)^2\right) \frac{u_1}{U_\infty} dx_2 \tag{3.37}$$

$$C_{\mathrm{Di}} = \frac{1}{\rho_\infty U_\infty^3} \int_0^\infty \tau \frac{\partial u_1}{\partial x_2} dx_2 \tag{3.38}$$

The energy and density thickness shape parameters H^* and H^{**} are defined in a similar manner as well.

$$H^* = \frac{\theta^*}{\theta} \tag{3.39}$$

$$H^{**} = \frac{\delta^{**}}{\theta} \tag{3.40}$$

To provide closure for equations 3.34 and 3.35 the following functional dependencies are assumed.

$$H^* = f(H_k, M_e, Re_\theta) \tag{3.41}$$

$$H^{**} = f(H_k, M_e) \tag{3.42}$$

$$C_f = f(H_k, M_e, Re_\theta) \tag{3.43}$$

$$C_{Di} = f(H_k, M_e, Re_\theta) \tag{3.44}$$

The kinematic shape parameter H_k is defined as:

$$H_k = \frac{H - 0.290M_e^2}{1 + 0.113M_e^2} \tag{3.45}$$

It is easy to see that for low speed subsonic flow, that $H_k = H$

3.3.2.1 Closure

Functional relationships for the additional parameters of C_f, C_{Di}, and H_k are needed to fully close the system. The following relationships from the Falkner-Skan one parameter profiles for laminar closure [8].

$$Re_\theta \frac{C_f}{2} = \begin{cases} -0.067 + 0.01977\frac{(7.4-H_k)^2}{H_k-1} & H_k \leq 7.4 \\ -0.067 + 0.022\big(1 - \frac{1.4}{H_k-6}\big)^2 & H_k \geq 7.4 \end{cases} \tag{3.46}$$

$$Re_\theta \frac{2C_{Di}}{H^*} = \begin{cases} 0.207 + 0.00205\big(4 - H_k\big)^{5.5} & H_k \leq 4 \\ 0.207 - 0.003\frac{(H_k-4)^2}{(1+0.02(H_k-4)^2)} & H_k \geq 4 \end{cases} \tag{3.47}$$

$$H^{**} = \Big(\frac{0.064}{H_k - 0.8} + 0.251\Big)M_e^2 \tag{3.48}$$

Functional relationships for C_f, C_{Di}, and H_k in transitional and turbulent flow are more involved and outside the scope of this thesis. More information about possible relationships can be found in [8].

3.4 Coupled Viscous-Inviscid Solution

Once a solution for the velocity distribution has been found via a panel method, the velocity profile can be used to numerically solve the boundary layer equations. From that solution, more accurate values of the drag forces on an airfoil can be found. This process of linking the two sets of equations is called viscous-inviscid coupling. There are several different methods of viscous-inviscid coupling that will be discussed below.

3.4.1 Direct Coupling

Direct coupling is the oldest and simplest method of coupling viscous-inviscid solutions. Once the potential flow has been solved for, the velocity profile is used to determine the solution to the boundary layer equations. This is a one-way coupling since the results from the potential solver flow in one direction only. A more advanced version of the direct coupling method involves adjusting the potential flow solver based on the results of the boundary layer solution. This two-way coupling can be accomplished by translating each panel in the direction normal to it's original orientation by specified fraction of the boundary layer height at that location. The solution process is then repeated until the amount the panel is translated such that it falls outside the viscous boundary layer region. This iterative process can have convergence issues and requires discretizing the domain during each iteration. The preferred method of coupling information from the boundary layer region with the inviscid region is through the use of a transpiration velocity. The concept of a transpiration velocity, first proposed by Lighthill is that the boundary layer effects can be simulated by imposing a non-zero normal velocity boundary condition on the inviscid solver [16]. The value of the transpiration velocity is determined from:

$$u_{2,trans} = \frac{d}{dx_1}(u_1|_{x_2=\delta}\delta^*) \tag{3.49}$$

For laminar attached flow, the size of the boundary layer grows in thickness along the x_2 direction. The interaction between the boundary layer and inviscid region is weak. However, as the flow approaches separation, directly coupled boundary layer solutions fail as the skin friction vanishes, leading to a singularity (termed the Goldstein singularity after the person who first described this issue)[5]. To get around this issue, a two equation boundary layer solution paired with one of the following methods can be used.

3.4.2 Quasi-Simultaneous

The quasi-simultaneous method, proposed by Veldman uses an interaction law to couple the solution from the boundary layer equations and the inviscid solution. The interaction law chosen is based off of thin airfoil theory and is used to approximate the inviscid region for the boundary layer solution. The quasi-simultaneous solution method can reach convergence very quickly and yields predictions within 1% of experimental results [22].

3.4.3 Simultaneous

The simultaneous method, like its name indicates, solves the boundary layer equations simultaneously with the inviscid flow field. Usually a global Newton method is used to solve the discretized set of equations. This method was popularized by Mark Drela and is used in XFOIL (created by Drela) [7]. It presents a robust and fast method for analysis of a coupled viscous-inviscid arbitrary airfoil.

3.5 XFOIL

XFOIL, an existing VII code was chosen to perform the analysis. This code was developed by Mark Drela, and uses the simultaneous method to couple the inviscid region with that of the boundary layer. In addition, it also has some other features that make it attractive for an optimization problem that might have inputs that span several different flow regimes. XFOIL can handle flows that are treated as solely inviscid, or a coupled viscous-inviscid region, laminar and turbulent flows including transition, separation, and reattachment bubbles, as well as both incompressible and compressible flows [7]. XFOIL provides accurate results well into the high-subsonic flow regime at a low computational cost. This efficiency paired with it's simple problem specification structure make it an ideal choice for automating the analysis process and coupling with a genetic algorithm optimization method.

3.6 Genetic Algorithm Settings

The various controls over the implementation of a genetic algorithm can greatly influence the quality and speed to convergence. From the No Free Lunch theorem, we know that there is no one optimal search method for all classes of problems. By extension, there is no one set of algorithm parameters that yield the best results (in both speed and solution quality) [6]. Therefore optimization parameters (given as functions of n, the number of parameters for a given airfoil family) were chosen based on rule of thumb estimates from literature [10] [13].

Parameter	**Value**
Population Size	$10n$
Elite Population	$0.05n$
Mutation Rate	0.03
Crossover Rate	0.75

Table 3.1: Genetic Algorithm Solver Input Parameters

Chapter 4

Results and Discussion

4.1 Introduction

A genetic algorithm optimization method was used to evaluate thousands of different possible parametric airfoil configurations for three main airfoil families with the goal of minimizing the objective (fitness) function (Equation 2.10) such that aircraft performance parameters were maximized per their weighted importance.

This approach differs from traditional optimal airfoil candidate searches in that it searches over a larger design space, evaluates each candidate airfoil over a range of conditions that have been weighted by their respective importance's, and that it searches for the best candidate that meets both its maximal range and endurance objectives. The results for each individual airfoil family are presented below.

4.1.1 NACA 4 Digit

The NACA 4 digit airfoil family converged the fastest to an optimal solution, finishing in 83 generations. The fitness score convergence for the NACA 4 digit series can be seen in Figure 4.1. This speed of convergence is most likely due to its limited design space which can be attributed to the fact that its governing parametric equations can only represent a limited amount of shapes when compared to the more general CST and PARSEC methods. Additionally, the NACA 4 digit airfoil series only needs three parameters to fully define its shape which is much fewer than the six and ten variables needed for the CST and PARSEC methods respectively.

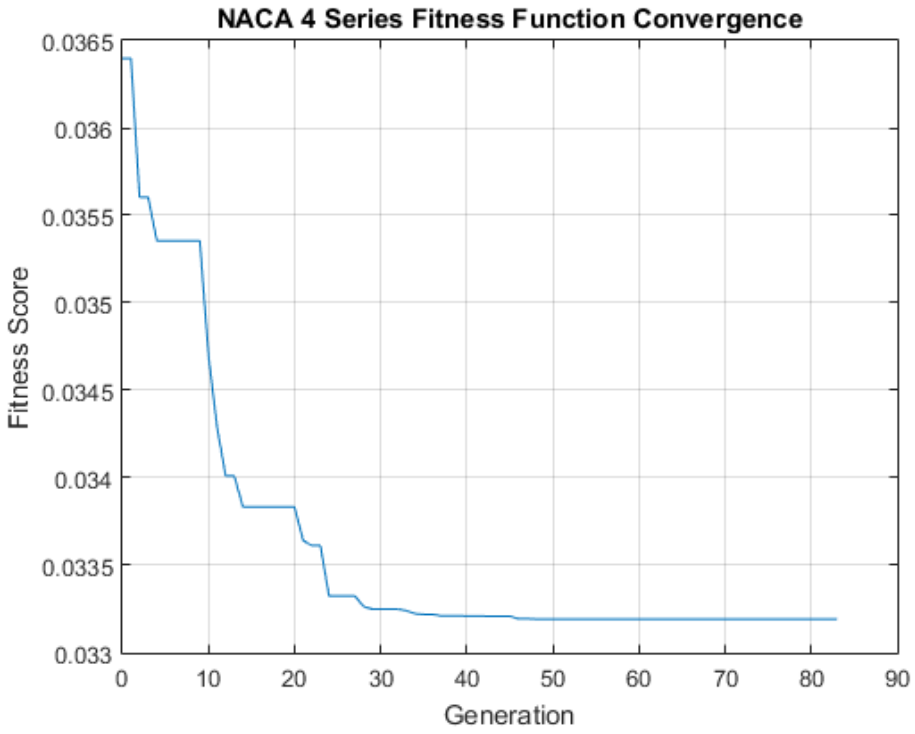

Figure 4.1: NACA 4 Series Fitness Function Score Convergence

The general evolution of the NACA 4 digit series can be seen in Figure 4.2. The airfoil shape adopts a heavily cambered shape, but after a few generations evolves to an airfoil that has a more subtle camber. This can be seen by how the upper surface of the

airfoil in generation 4 becomes higher in later generations before falling back to just below it's original location. The lower surface also goes through a similar refinement process by which a large amount of camber is added and then slowly removed until an optimal solution is found.

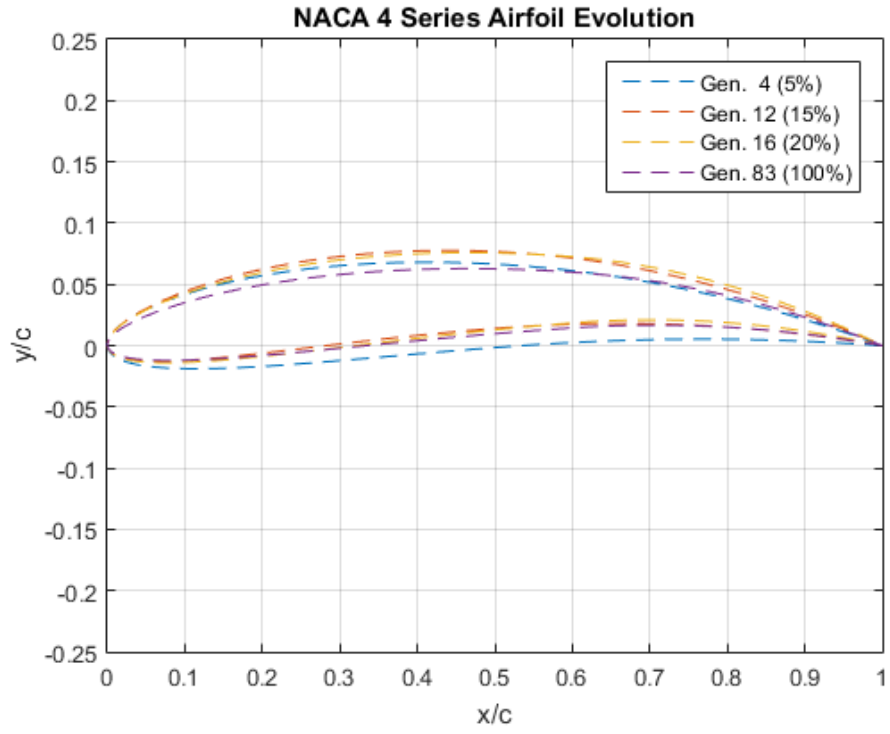

Figure 4.2: Evolution of Optimal NACA 4 Series Airfoil

From Figure 4.3 the shape of the airfoil can be seen. It's high level of camber is noticeable as the leading edge appears to be drooped. Additionally, the high camber of the lower surface near the trailing edge is noticeable. When compared to commonly used NACA 4 digit series airfoil configurations such as the NACA 2412 one can see that the L/D ratio for the optimized airfoil is several times larger indicating a better performance than a regular "off the shelf" configuration. The performance parameters for each condition of the optimal airfoil can be found in Tables 4.1-4.2.

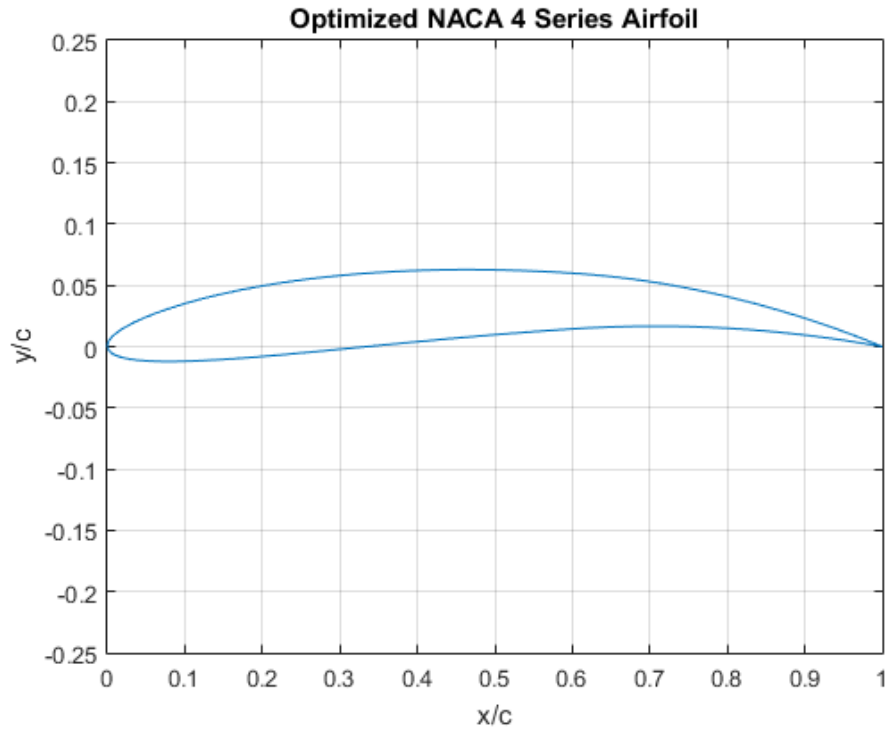

Figure 4.3: Final Optimized NACA 4 Series Airfoil

ID	c_l	c_d	c_l/c_d	C_L	C_D	C_L/C_D	$C_L^{\frac{3}{2}}/C_D$
1	0.65	0.004	148	0.64	0.02	39	31
2	0.65	0.005	136	0.64	0.02	38	30
3	0.64	0.006	103	0.63	0.02	35	28

Table 4.1: Optimized NACA 4 Series Endurance Mission Performance

ID	c_l	c_d	c_l/c_d	C_L	C_D	C_L/C_D	$C_L^{\frac{3}{2}}/C_D$
1	0.70	0.004	162	0.69	0.02	38	31
2	0.71	0.005	150	0.69	0.02	37	31

Table 4.2: Optimized NACA 4 Series Range Mission Performance

4.1.2 CST

The CST airfoil optimization took 113 generations before it converged on an optimal solution. This is slightly longer than the NACA 4 series, again due to it's larger available

design space. A chart of the CST airfoil's fitness function convergence can be seen in Figure 4.4.

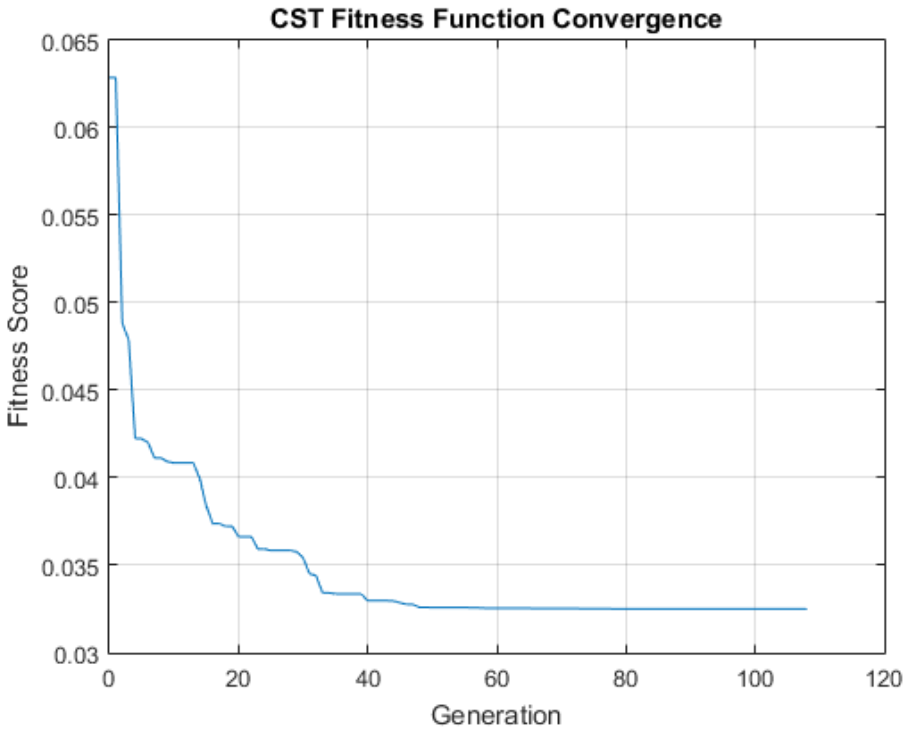

Figure 4.4: CST Fitness Function Score Convergence

The evolution of the CST airfoil followed a similar pattern to that of the NACA one in that it started out with a high degree of camber and high thickness and the gradually refined those values until it reached convergence. The evolution of the CST airfoil can be seen in Figure 4.5.

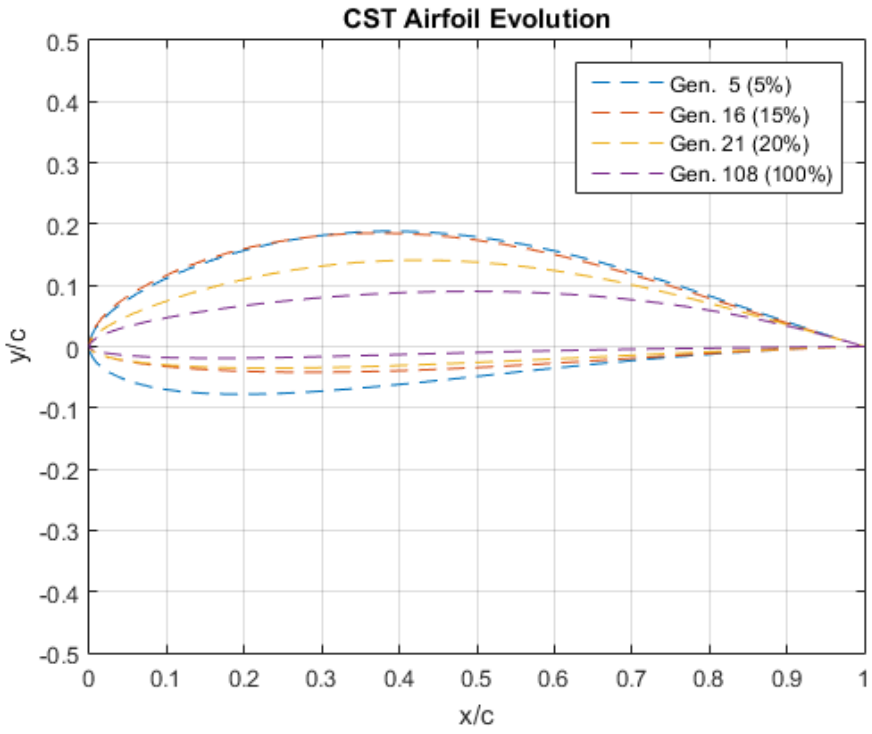

Figure 4.5: Evolution of Optimal CST Airfoil

The final optimal CST airfoil can be seen in Figure 4.6. It is an asymmetric airfoil with a relatively high amount of camber with it's peak located about 50% of the chord. It differs from the NACA airfoil it that is has a much flatter lower surface with a just barely noticeable amount of camber.

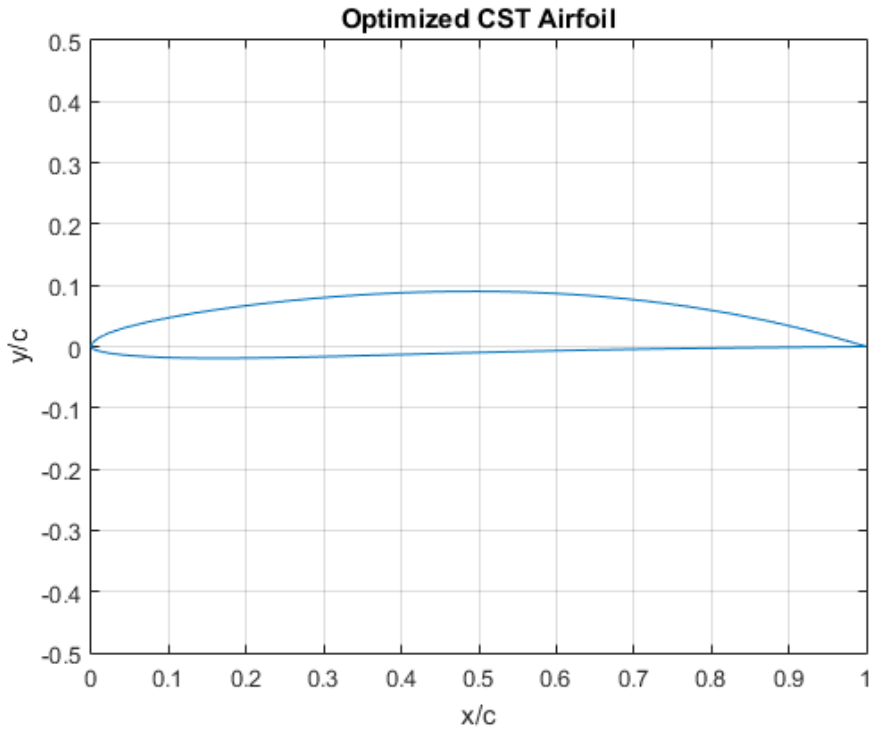

Figure 4.6: Final Optimized CST Airfoil

The performance parameters for each condition of the optimal airfoil can be found in Tables 4.3-4.4. One can see that the performance of the optimized CST airfoil is slightly better than that of the NACA one when comparing L/D and $C_L^{\frac{3}{2}}/C_D$, which is due to the significantly lower amount of induced drag that the NACA airfoil has from the higher amount of lift it generates.

ID	c_l	c_d	c_l/c_d	C_L	C_D	L/D	$C_L^{\frac{3}{2}}/C_D$
1	0.53	0.004	138	0.52	0.01	44	32
2	0.52	0.004	129	0.51	0.01	43	31
3	0.59	0.006	97	0.58	0.01	36	27

Table 4.3: Optimized CST Endurance Mission Performance

ID	c_l	c_d	c_l/c_d	C_L	C_D	L/D	$C_L^{\frac{3}{2}}/C_D$
1	0.55	0.004	143	0.55	0.01	43	32
2	0.55	0.004	131	0.54	0.01	42	31

Table 4.4: Optimized CST Range Mission Performance

4.1.3 PARSEC

The PARSEC airfoil optimization took the highest amount of generations to converge at 216 generations. It's fitness function convergence as a function of generation can be seen Figure 4.7. This is unsurprising since the PARSEC airfoil had the most amount of variables needed to define the airfoil geometry (10 total variables since the the airfoil was assumed to have a sharp trailing edge).

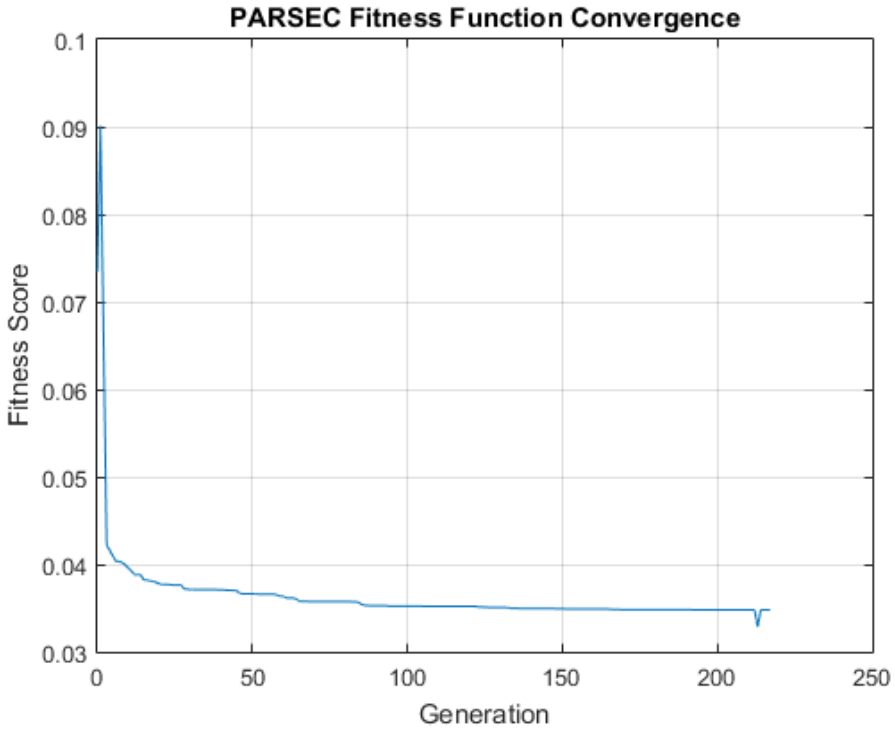

Figure 4.7: PARSEC Fitness Function Score Convergence

The shape of the PARSEC airfoil was quite different than either the NACA or CST as can be seen by its evolution in Figure 4.8. It starts off as a highly cambered airfoil with near constant thickness and eventually evolves into a thin tadpole shaped airfoil.

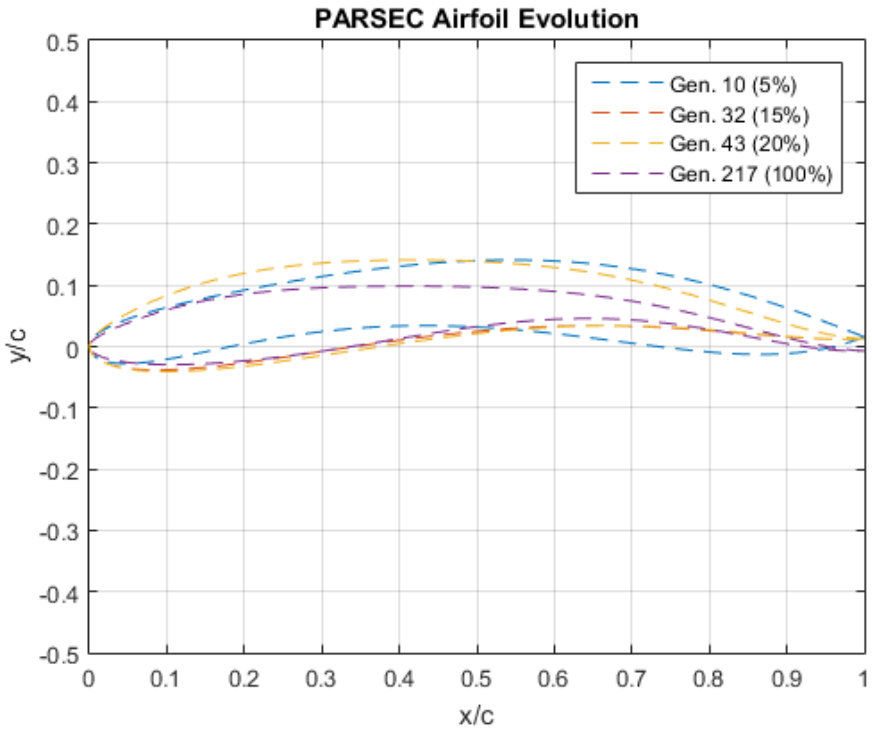

Figure 4.8: Evolution of Optimal PARSEC Airfoil

The final PARSEC airfoil can be seen in Figure 4.9. It is unique in that that its trailing edge thins out significantly for an extended portion of the chord length. This extended portion makes it visually interesting but most likely unfeasible for an actual load bearing aero-structure. The performance parameters for each condition of the optimal airfoil can be found in Tables 4.5-4.6.

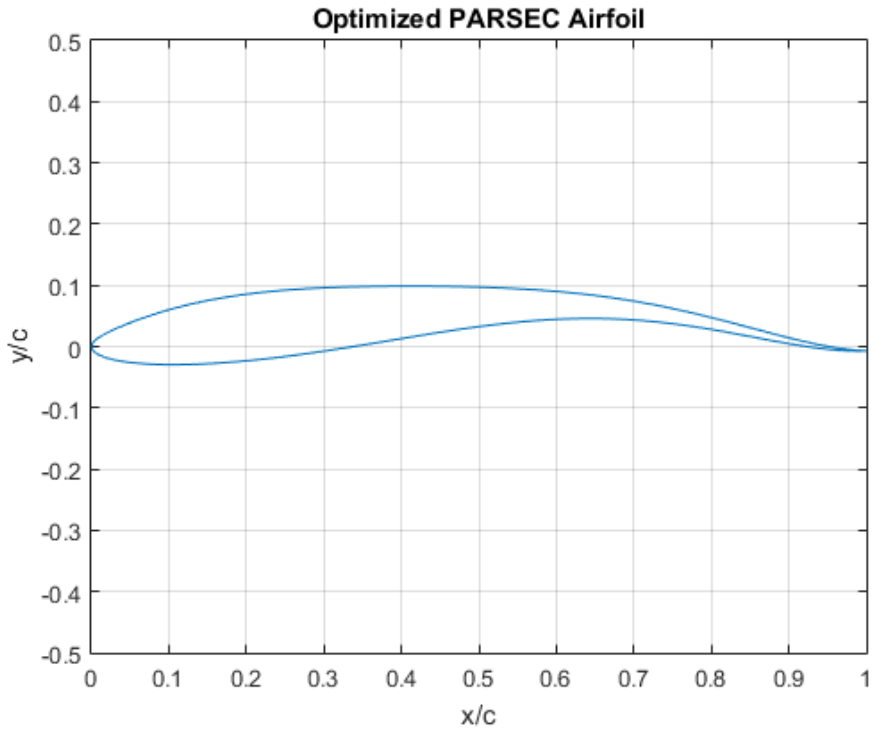

Figure 4.9: Final Optimized PARSEC Airfoil

ID	c_l	c_d	c_l/c_d	C_L	C_D	C_L/C_D	$C_L^{\frac{3}{2}}/C_D$
1	0.69	0.005	139	0.67	0.02	37	30
2	0.69	0.006	120	0.68	0.02	35	29
3	0.70	0.008	83	0.68	0.02	31	25

Table 4.5: Optimized PARSEC Endurance Mission Performance

ID	c_l	c_d	c_l/c_d	C_L	C_D	C_L/C_D	$C_L^{\frac{3}{2}}/C_D$
1	0.75	0.005	161	0.73	0.02	36	31
2	0.76	0.005	139	0.74	0.02	34	29

Table 4.6: Optimized PARSEC Range Mission Performance

4.2 Comparison

All three final airfoils have relatively similar performance scores (Table 4.7) despite their differences in geometry (see Figure 4.10). In general, all three airfoils feature an asym-

metric design that is heavily cambered with the maximum camber located about $0.4c$-$0.5C$. However, one airfoil had the smallest objective score, making it the best suited airfoil when evaluated by the established rubric. This airfoil is the final iteration of the CST geometry. The other two airfoil candidates produced enough lift that the amount of induced drag was significantly increased which subsequently decreased their overall performance. The CST on the other hand, had a lower sectional drag coefficient across all conditions leading to a better set of scores. This makes the CST airfoil the best choice for the nominal HALE UAV that is being designed.

Airfoil	Score
NACA	0.033193
CST	0.032511
PARSEC	0.034791

Table 4.7: Final Airfoil Scores

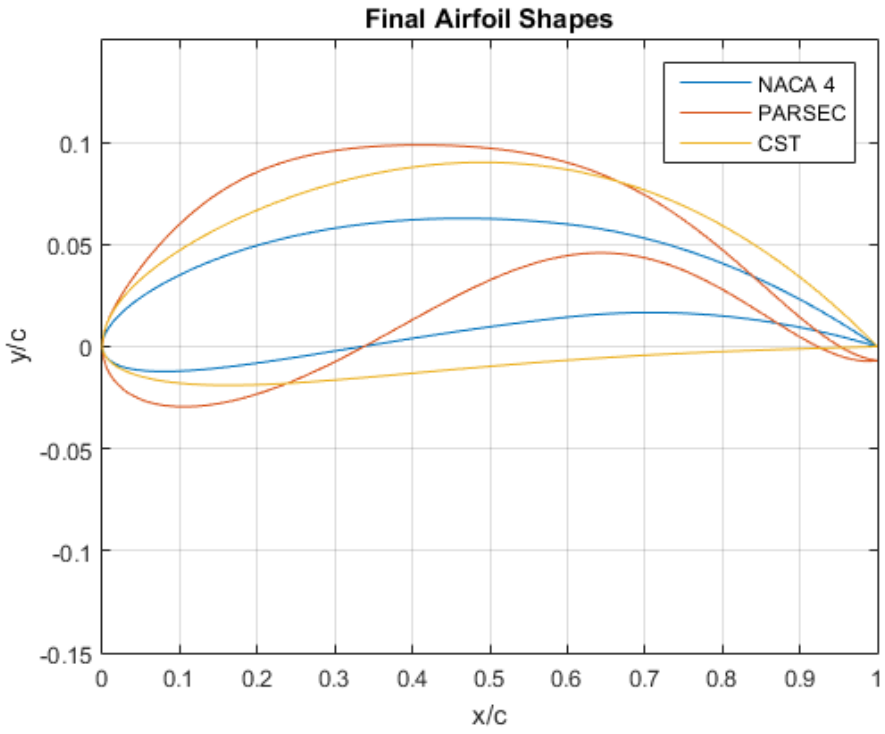

Figure 4.10: Final Airfoil Shapes

Chapter 5

Conclusion

The goal of this thesis was to find the best possible airfoil design for a HALE type UAV. The best, or optimal airfoil choice was defined as the one that maximized both the endurance and range over the nominal set of operational conditions, which meant maximizing the L/D and $L^{\frac{3}{2}}/D$ ratios. To find the value of these ratios, the aerodynamics of the airfoil needed to be analyzed. Each airfoil configuration was analyzed using a coupled viscous-inviscid method that blended potential theory and the panel method with a numerical solution to Prandtl's viscous boundary layer to produce good engineering solutions for the pressure and velocity fields. From this solution method, the lift and drag forces for a given airfoil and flight condition could be found and from there, the L/D and $L^{\frac{3}{2}}/D$ ratios could be found. The fitness score of the airfoil candidate was then computed using Equation 2.10. A single parameter fitness function was used to simplify the approach. To reduce the multiple objectives into one objective function, a weighted approach was used. Characteristic weights based on their importance were assigned to each objective, from which a weighted fitness function score could be computed. A genetic algorithm then used this weighted score as the parameter to be minimized by finding the vector of parameters that govern the shape of the airfoil. To accomplish this minimization goal, a MATLAB script was used to couple the VI

solver with the genetic algorithm. This process resulted in finding an airfoil that provides the best blend of performance characteristics when evaluated against the mission condition matrix. This approach was used for three separate parametric airfoil families. These three airfoil families were chosen since together, they provide for sufficient coverage of the possible design configurations.

The approach used was original in that it evaluated each candidate airfoil with a holistic method that attempted to balance multiple objectives across multiple conditions each with their own level of importance in a simplified and efficient manner. This difference is important because it searches for the airfoil configuration that is best suited for a typical mission rather than any one single segment of that mission. Additionally, it searched over a wider, more comprehensive design space than other optimizations had searched. By sweeping over a larger design space, it can be assumed that all reasonable airfoil configurations were included in the optimization. In addition, since the analysis portion of the solution used a VI method, it was able to find an optimal solution in a computationally efficient method. This is a huge advantage over more traditional CFD based approaches.

Any kind of aerodynamicist, hydro-dynamicist or large program manager can benefit from the analysis and optimization method presented in this thesis to help make large configuration decisions at the beginning of the engineering process. The efficiency of the method allows for many thousands of options to be evaluated quickly and accurately. In addition, the method can be expanded to include more objectives, constraints, or physical phenomena. This flexibility makes it very effective in performing initial scoping and trade studies, which in turn accelerates the detail design and analysis process such that new products can be brought to market more easily.

5.1 Further Work

This research presented a high level method to find an optimal airfoil for a nominal UAV design. There are several refinements and changes outlined below that can be implemented to improve the solution and find a better design:

1. Present more robust justification for the mission weights used in Tables 2.2-2.3 and in Equation 2.10.
2. Fine tune genetic algorithm parameters.
3. Use a multi-objective genetic algorithm instead of weighted single parameter optimization.
4. Expand the optimization problem such that the optimal finite wing, rather than airfoil is the goal. Do this by including parameters such as:
   (a) Wingspan.
   (b) Chord length.
   (c) Leading and trailing edge sweep angle.
   (d) Wing twist.
   (e) Airfoil blending between root and wingtip.
5. Add more objectives (ex maximize flight envelope, minimize wing volume).
6. Expand the VI calculation to include the full aircraft.

References

[1] John David. Anderson. *Introduction to Flight*. McGraw-Hill Education, 2015.

[2] *Applied Aerodynamics: A Digital Textbook*. Stanford, CA, Jan. 2007.

[3] Ashok D. Belegundu and Tirupathi R. Chandrupatla. *Optimization concepts and applications in engineering*. Cambridge University Press, 2014. URL: http://www2.mae.ufl.edu/haftka/eoed/protected/Belegundu-chapt11.pdf.

[4] Kulfan M. Brenda. "A Universal Parametric Geometry Representation Method – "CST"". In: *45th AIAA Aerospace Sciences Meeting and Exhibit*. Reno Nevada, 2007. DOI: 10.2514/6.2007-62. URL: http://brendakulfan.com/docs/CST2.pdf.

[5] E.G.M. Coenen, A.E.P. Veldman, and G Patrianakos. "QUASI-SIMULTANEOUS VISCOUS-INVISCID INTERACTION FOR THREE-DIMENSIONAL TURBULENT WING FLOW". In: (). URL: http://www.math.rug.nl/~veldman/preprints/ICAS-CPV.pdf.

[6] Wolpert D.H. and Macready W.G. "No Free Lunch Theorems for Optimization". In: *IEEE Transactions on Evolutionary Computation* 1.1 (1997), pp. 67–82. DOI: 10.1109/4235.585893. URL: https://ti.arc.nasa.gov/m/profile/dhw/papers/78.pdf.

[7] Mark Drela. *XFOIL: An Analysis and Design System for Low Reynolds Number Airfoils*. Cambridge, MA. URL: http://web.mit.edu/drela/Public/papers/xfoil_sv.pdf.

[8] Mark Drela and Michael B. Giles. "Viscous-inviscid analysis of transonic and low Reynolds number airfoils". In: *AIAA Journal* 25.10 (1987), pp. 1347–1355. DOI: 10.2514/3.9789. URL: http://www2.coe.pku.edu.cn/tpic/201172015638907.pdf.

[9] Jr. Francis Gary Powers. *fgp-u2*. [Online; accessed March 7, 2017]. URL: http://garypowers.org/wp-content/gallery/slideshow-photos/fgp-u2.jpg.

[10] John Grefenstette. "Optimization of Control Parameters for Genetic Algorithms". In: *IEEE Transactions on Systems, Man, and Cybernetics* 16.1 (1986), pp. 122–128. DOI: 10.1109/tsmc.1986.289288.

[11] James Hasik. *Affordably Unmanned: A Cost Comparison of the MQ-9 to the F-16 and A-10, and a Response to Winslow Wheeler's Criticisms of the Drone*. June 2012. URL: http://www.jameshasik.com/weblog/2012/06/affordably-unmanned-a-cost-comparison-of-the-mq-9-to-the-f-16-and-a-10-and-a-response-to-winslow-whe.html.

[12] *How the Genetic Algorithim Works*. [Online; accessed March 10, 2017]. Mar. 2017. URL: https://www.mathworks.com/help/gads/how-the-genetic-algorithm-works.html.

[13] Kenneth A. De Jong and William M. Spears. "An analysis of the interacting roles of population size and crossover in genetic algorithms". In: *Parallel Problem Solving from Nature Lecture Notes in Computer Science* (1991), pp. 38–47. DOI: 10.1007/bfb0029729.

[14] Sungki Jung et al. "An Implementation of Self-Organizing Maps for Airfoil Design Exploration via Multi-Objective Optimization Technique". In: *Journal of Aerospace Technology and Management* 8.2 (2016), pp. 193–202. DOI: 10.5028/jatm.v8i2.585. URL: http://www.scielo.br/pdf/jatm/v8n2/1984-9648-jatm-8-2-0193.pdf.

[15] Arnold M. Kuethe and Chuen-Yen Chow. *Foundations of aerodynamics: bases of aerodynamic design*. J. Wiley, 2000.

[16] M.J. Lighthill. "On displacement thickness". In: *Journal of Fluid Mechanics* 4 (1958), pp. 383–392. DOI: 10.1.1.208.3645.

[17] H. William Mason. *Applied Computational Aerodynamics*. Feb. 1998. URL: http://www.dept.aoe.vt.edu/~mason/Mason_f/CAtxtChap4.pdf.

[18] K. Ambar Mitra. *Panel Method*. URL: http://www.public.iastate.edu/~akmitra/aero361/design_web/panel.

[19] Lelanie Smith. "An Interactive Boundary Layer Modelling Methodology for Aerodynamic Flows". University of Pretoria, 2011. URL: http://www.crses.sun.ac.za/files/research/completed-research/solar/Smith_Lelanie_Masters.pdf.

[20] R. Charles Smith. *Introduction to Graduate Fluid Mechanics*. Self, 2016.

[21] Helmut Sobieczky. "Parametric Airfoils and Wings". In: *Notes on Numerical Fluid Mechanics (NNFM) Recent Development of Aerodynamic Design Methodologies* 68 (1999), pp. 71–88. DOI: 10.1007/978-3-322-89952-1_4. URL: http://www.as.dlr.de/hs/h-pdf/H141.pdf.

[22] A.E.P. Veldman. "Boundary Layers in Fluid Dynamics". 2012. URL: http://www.math.rug.nl/~veldman/Colleges/grenslaag/BoundaryLayers2012.pdf.

Curriculum Vitae

Joshua B. Okrent was born on May 6, 1992 to Aaron and Aileen Okrent in Bellevue, Washington. Joshua attended Interlake High School in Bellevue, Washington where he was an Advanced Placement (AP) State Scholar. He also a diploma through the International Baccalaureate Program. Joshua graduated from Lehigh University in 2014 with a Bachelor's of Science in Mechanical Engineering. He also minored in Aerospace Engineering and Applied Mathematics. While a student at Lehigh, Joshua held several internships in the aerospace industry, first as a manufacturing engineering intern at Giddens Aerospace in Everett, Washington and then at Electroimpact in Mukilteo, Washington as a mechanical engineering intern. Upon graduating he began working for The Boeing Company, first as a satellite ground support equipment mechanical design engineer in El Segundo, California. After working as a design engineer, he transitioned to a flight test instrumentation engineering position with The Boeing Company in Seattle, Washington. While a flight test engineer, he participated in test flights for the KC-46A Pegasus aerial refueling tanker. Joshua currently works as a mechanical engineer in the research and design group of TerraPower, a small nuclear engineering company focused on advanced reactor concepts in Bellevue, Washington.